Fuel 385 (2025) 134128

Contents lists available at ScienceDirect

Fuel

journal homepage: www.elsevier.com/locate/fuel

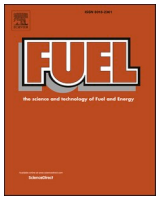

Full Length Article

Numerical investigation of the NO_X emissions of a perfectly premixed NH_3-H_2 flame at moderate pressure levels

R. Meloni [a,*], A. Valera-Medina [b], G. Babazzi [a], E. Pucci [a], S. Castellani [c], A. Andreini [c]

[a] Baker Hughes, Florence, Italy
[b] Cardiff University School of Engineering, Cardiff, Wales, UK
[c] Department of Industrial Engineering, University of Florence, Italy

ARTICLE INFO

Keywords:
Ammonia combustion
Hydrogen combustion
NOx emissions
Thickened flame model
Large Eddy simulation
Reaction mechanism

ABSTRACT

Blends of green hydrogen-ammonia for Gas Turbines (GT) are gaining more and more interest, as their carbon neutrality can abate CO_2 emissions. Such fuel mixture could be particularly effective since the low reactivity of ammonia can compensate the aggressive properties of hydrogen in terms of both flame speed and low heating value, reducing the re-design effort of the traditional dry-low emission combustors. From the environmental perspective, the main drawback is represented by the NO_x emissions, mostly related to the fuel-bound pathway activated by the cracking of NH_3: its mitigation requires the proper control of the equivalence ratio of the blend along the selected ratio of ammonia and hydrogen in the fuel mixture. Additionally, at relevant GT conditions, a moderate benefit for NO_x reduction can be played by the pressure rise.

In this work, the effect of the operating pressure onto the NO_x emission is investigated numerically in the range 1.1–2 bar along a perfectly premixed mixture of 25 % NH_3 – 75 % vol. H_2 at constant equivalence ratio, leveraging the corresponding experimental data. The tests employ a radial swirler whose performances are measured not only in terms of NO_x but also through detailed flame imaging. The latter is used to evaluate the accuracy of a Thickened Flame Model (TFM) in predicting the flame shape and position. The TFM is based on a skeletal mechanism consisting of 27 species that embeds the OH* to directly compare the numerical line of sight with the images from the experiment and the NO_x chemistry as well. Regarding the NO_x, the numerical results show a reasonable accuracy: not only can the overall flame length be captured but also a quantitative estimation can be retrieved from the numerical model. Lastly, the impact onto NO_x of the hydrogen preferential diffusion related to the flame curvature is discussed.

1. Introduction

The use of green ammonia for decarbonizing the energy and power generation sectors is gaining more and more interest since the penetration of electricity produced by renewable sources is expected to cover a significant share of the total consumption in the next decades. Even more effective can be its coupling with hydrogen, always produced leveraging the excess of renewable electricity, because their chemical properties (flame propagation, low heating value and ignition delay time) are somehow complementary [1–3]. The main concerns related to the use of ammonia as fuel remain the toxicity, corrosivity and, more importantly from an environmental perspective, the high NO_x emission [4,5]. Dealing with NH_3-H_2 blends, traditional GT combustors are expected to face significant changes to operate safely within a low-NO_x window. While the modern architectures rely on the dry-low NO_x technology that implies the premixing of the fuel to achieve single-digit emissions, both ammonia and hydrogen are not fully compatible with this strategy. It is demonstrated that the oxidation of ammonia in a lean-regime leads to the highest NO_x emission, hence the combustion has to be performed under fuel-rich conditions instead [6,7]. Conversely, the premixing of hydrogen exposes the burner to the risk of flashback, especially when operated at elevated pressure and pre-heated air temperature. Another degree of freedom is the ammonia-to-hydrogen ratio within the fuel blend that can influence the choice of the burner architecture [8]: to have the maximum flexibility, the combustor is expected to burn fuel mixtures ranging from high-NH_3 to high-H_2 contents with or without blends with natural gas. Lastly, the benefit of the higher and higher pressure ratio of the modern GTs needs to be proved for the NO_x reduction: the fuel-bound formation path related to the ammonia shows

* Corresponding author.
E-mail address: roberto.meloni@bakerhughes.com (R. Meloni).

https://doi.org/10.1016/j.fuel.2024.134128
Received 1 August 2024; Received in revised form 13 December 2024; Accepted 15 December 2024
Available online 24 December 2024

Nomenclature

Symbols

D	Species diffusivity [m^2/s]
E	Efficiency function [-]
F	Thickening factor [-]
k	Flame curvature [-]
s_l^0	Laminar Flame Speed [m/s]
W	Molecular weight [kg/mol]
Y	Mass Fraction [-]
Z	Elemental mass fraction [-]

Greek

α	Combustion model constant
β	Model constant
φ	Vector of the species mass fractions
Φ	Equivalence ratio
Γ	Combustion model function
∇	Gradient operator
Ω	Flame sensor
$\dot{\omega}$	Reaction Rate [kg/m^3-s]

Subscripts / Superscript

0	Refers to the flame without thickening
1	Refers to the flame with thickening
l	Laminar
max	Referred to the thickening factor
T	Referred to a tabulated value

Acronyms

CFD	Computational Fluid Dynamics
CFL	Courant-Friedrichs-Lewy number
CRN	Chemical Reactor Network
FGM	Flamelet Generated Manifold
FR	Finite Rate
FTT	Flow Through Time
GT	Gas Turbine
IRZ	Inner Recirculating Zone
LBV	Laminar Burner Velocity
LES	Large Eddy Simulation
LFS	Laminar Flame Speed
LFT	Laminar Flame Thickness
N	Number of points in the flame thickness
PaSR	Partially Stirred Reactors
PIV	Particle Image Velocimetry
RANS	Reynolds Average Navier-Stokes
RoP	Rate of Production
TFM	Thickened Flame Model
UDF	User Defined Function

a NO_x reduction till moderate levels of the operating pressure [9] while the thermal-NO pathway should get worse with the pressure rise, even if this mechanism could be design dependent [10,11]. To better understand the real potential of NH_3-H_2 blends, such challenges have still to be investigated at different levels of research, from lab scale to the validation in real engine conditions. As effectively discussed in the recent work of Ditaranto and Saanum [12], where a complete literature review of the most recent experimental studies of high pressure ammonia combustion, a gap in knowledge exists regarding the sensitivity of NOx emissions to pressure levels beyond 4 bar, with lack of experimental data for the typical ammonia blends at relevant engine operating conditions. The study investigates swirl-stabilized combustion of decomposed ammonia, exploring the whole range (from pure NH3 to H2/N2) up to 10 bar analyzing the role of equivalence ratio and residence time. One of the most significant findings is the observation that the transition pressure beyond which its effect on NOx emissions vanishes (at least up to the maximum level investigated in the study, 10 bar) is not an absolute value but it is a function of equivalence ratio, H2/NH3 ratio and residence time. The minimum transition pressure observed is 5 bar, confirming that the most significant NOx pressure effects are observed in the range 1–3 bar. Also N2O shows a peak for pressure below 5 bars, almost vanishing for higher pressure.

Also from the numerical standpoint and specifically from the CFD side, there is still a considerable amount of work to do, especially in terms of fuel-bound NO_x prediction. Focusing on the latter aspect, several approaches characterized by different levels of complexity can be found in literature. Here the attention will be focused on those that can be potentially applied for hardware design intent. A quite common strategy is the coupling of the CFD solution with a dedicated CRN that allows the assessment of NO_x to be performed in a post-processing step: the works from Mikulčić et al. [13] and Chaturvedi et al. [14] are examples of this kind. Both studies leverage RANS turbulence model with a finite-rate closure to investigate perfectly premixed conditions in a swirled burner. The former research is focused on a premixed NH_3-CH_4 fuel gas while the latter on a blend of NH_3 (70 % vol) – H_2 (30 % vol). The CRN is leveraged in both works to test several chemistry sets. The main outcome from these investigations is quite similar: the comparison with the experimental data reveal that a significant NO_x overprediction cannot be avoided in the lean-regime while a satisfactory agreement can be achieved only for rich mixtures. The same trend is found for all the chemical mechanisms employed in these works. The nature of the CRNs as well as of all the reduced order models cannot allow quantitative assessment of pollutant emissions but can surely help in the identification of chemical mechanisms offering superior performance. The fact that several mechanisms show the same NO_x prediction trend and the same order of magnitude of discrepancy against the data demonstrate that the path toward a fully comprehension of the topic is still far from be achieved.

An interesting methodology to calculate the NO_x emission directly from the CFD simulation along pre-tabulated combustion models is based on the decoupling of the NO/NO_2 chemistry from the rest of the solution. This can be done solving dedicated transport equations associated to these species whose source terms are stored as a function of the primitive scalars, i.e. progress variable and mixture fraction. This approach allows the separation of the NO_x formation time scale from the characteristic time scale of the species employed to define the progress variable. It's the case presented in An et al. [15] and Wang et al. [16]. In the first work, a FGM model is run in a LES context to investigate rising percentages of NH_3 blended with CH_4 feeding a perfectly premixed swirler. The benefit of the decoupling strategy against the tabulated NO is measured comparing both trends with experimental data. Despite that, when the NH_3 volume fraction exceeds 20 % in the fuel, the transported NO significantly exceeds the experimental measures despite a very good prediction of both the velocity field and the mean position of the flame inside the combustor. The same numerical strategy is adopted in the second research paper investigating a non-premixed flame burning a gas obtained from the NH_3 cracking. Two levels of ammonia are considered, 56 % and 75 %, respectively. An interesting finding comes from the comparison of the predicted NO radial profiles with the measured ones, taken at several axial positions along the flame tube: while an excellent agreement is obtained for the radial profiles close to the burner exit, a gradual deterioration can be observed moving close to the combustor exit, till a final overprediction of about 50 % at the outlet. Another interesting investigation relying on LES/FGM models is

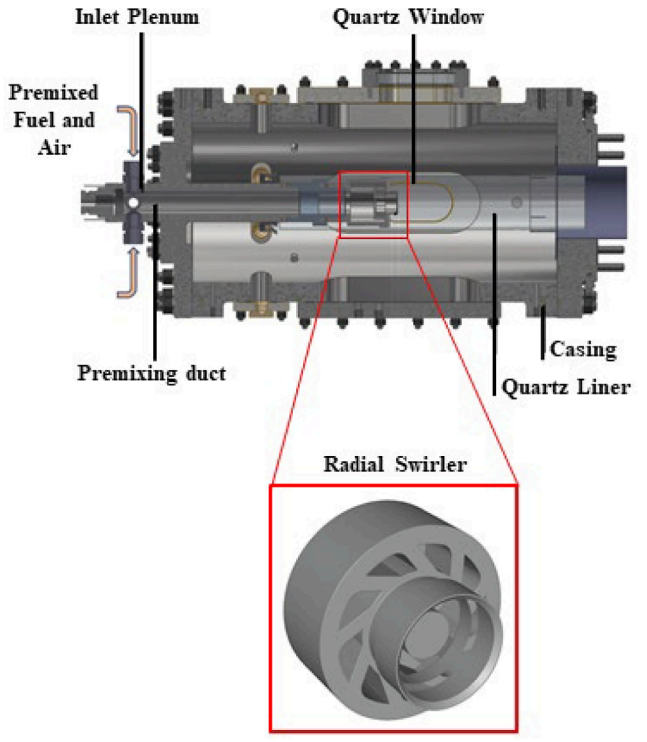

Fig. 1. Pressurized Test Rig with close up of the radial swirler and its tip.

presented by Honzawa et al. [17] where the effect of the heat losses on pollutant emissions (NO_x and CO) is specifically investigated in a perfectly premixed swirler fed with a blend of NH_3/CH_4. No decoupling strategy is adopted since the species concentrations are directly evaluated from the pre-tabulated table. Nevertheless, the latter is built considering the heat loss effect onto the species mass fractions. The comparison of the results obtained through this approach against the adiabatic flamelets shows a significant improvement of NO_x prediction demonstrating that the heat loss is a parameter that cannot be neglected. Despite that, the distance from the experimental data remains considerable: NO_x are up to 5 times higher than the data in the lean regime and up to 1.5 times in the rich one with the minimum discrepancy across the stoichiometric conditions. Such trend is confirmed for 4 different chemical mechanisms investigated in this study.

Rising with the computational effort, another numerical strategy is represented by those combustion models relying on the transport of all the primitive variables, the so-called species transport models where a transport equation is associated to each chemical species. The application of such approach for the prediction of NO_x can be particularly expensive since most of its chemistry has to be preserved to achieve satisfactory results, even when reduced mechanisms are adopted. Xiao et al. [18] adopt this strategy implementing the PaSR combustion model in a LES context. A reduced chemistry is specifically derived trying to contain the computational time to simulate the same perfectly premixed burner investigated in [17] burning a fuel made of NH_3/H_2, both at 50 % vol. Four simulations are performed with the equivalence ratio rising from 0.43 to 0.56. The discrepancy of the numerical results with the data gets lower and lower rising with the equivalence ratio: while the predicted NO_x are more than twice at the lowest equivalence ratio investigated, the difference at the highest is practically negligible. This is an important achievement since the high emissions produced in the lean regime are usually never captured with such accuracy, demonstrating the improved prediction capability of the species transport models. One of the biggest challenge associated to the usage of this numerical strategy is the derivation of skeletal mechanisms able to drastically reduce the computational effort without compromising the accuracy of the solution, especially in terms of NO_x prediction. This achievement could potentially break the barrier represented by the extremely high cost associated to the investigation of ammonia as fuel in industrial geometries and at relevant GT operating conditions. In this context, the present work wants to make a step forward in this path presenting the application of a species-transport based model leveraging a chemistry set reduced *ad-hoc*. The simulations will investigate a semi-industrial radial swirler, operated in a fully premixed mode with a blend of ammonia/hydrogen for which the experimental data will be used to both validate the NO_x emission model and verify the flame shape/morphology at different levels of operating pressure. The document is organized into three main sections. The first will describe the test bench and the details in terms of investigated operating conditions. The second will present all the different aspects related to the numerical models while the last one will shows the main results with a strong focus on the analysis of the NO_x.

Table 1
Experimental data of the three operating conditions investigated.

	TP1	TP2	TP3
Fuel Gas	75 % H_2 – 25 % NH_3 % vol.		
Air Temperature	500 K		
Equivalence Ratio	0.287		
Pressure [bar]	1.1	1.5	2.0
Air Flow Rate [g/s]	13.0	17.73	23.98
NH_3 Flow Rate [g/]	0.205	0.28	0.382
H_2 Flow Rate [g/s]	0.073	0.099	0.132
Flame Speed [m/s]	0.115	0.079	0.06
Flame Thickness [mm]	1.46	1.33	1.28

1.1. Test rig and investigated operating conditions

The tests are executed in a high-pressure facility with optical access, shown in Fig. 1 [19,20]. The flame tube is a quartz cylinder and it can be visualized during the tests thanks to optical windows mounted on the external casing of the rig. The ammonia-hydrogen blend is created well upstream the radial swirler thanks to a premixing duct where it mixes with air: the mixture can be considered as perfectly premixed when it reaches the primary zone of the combustor. The fuel and air mass flow rates are metered by specific Coriolis mass flow controllers ensuring an accuracy of ± 0.35 % of the target value. The flame is stabilized within the IRZ created by the radial swirler thanks to its relatively high swirl number equal to 0.8.

Exhaust gases for emission measurements are sampled downstream the metal liner placed right downstream the quartz tube at approximately 540 mm from the dome plate. The water content, residual oxygen, unburned NH3 and NOx (NO and NO2) are measured through a bespoke Emerson CT5100 Quantum Cascade Laser analyzer at a frequency of 1 Hz and an operating temperature of about 460 K. Unfortunately, N2O representing another source of greenhouse emissions at very lean conditions (like the ones that will be investigated in this work) couldn't be measured. NOx and NH3 measurements are performed in hot and wet conditions using a heated probe to avoid any water condensation from the sampling section till the instrumentation.

OH* chemiluminescence is acquired through a high-speed camera (LaVision Image Intense CCD) connected to an image intensifier and UV lens with a 310 nm narrow bandpass filter. OH* maps are created using the same gain (equal to 5), exposure time (10 us) and acquisition frequency (4000 Hz) for all the operating conditions here presented. Each image represents the average of 2000 samplings.

The temperature at several locations is recorded through K and R thermocouples. For each test conditions, the final profiles represent a time-average of 120 s. Thermocouples are installed along the quartz tube, the dome plate and the burner tip as well as at the exhaust. The measures are corrected to take convective and radiative heat transfer into account. Regarding the quartz, the temperature is measured at

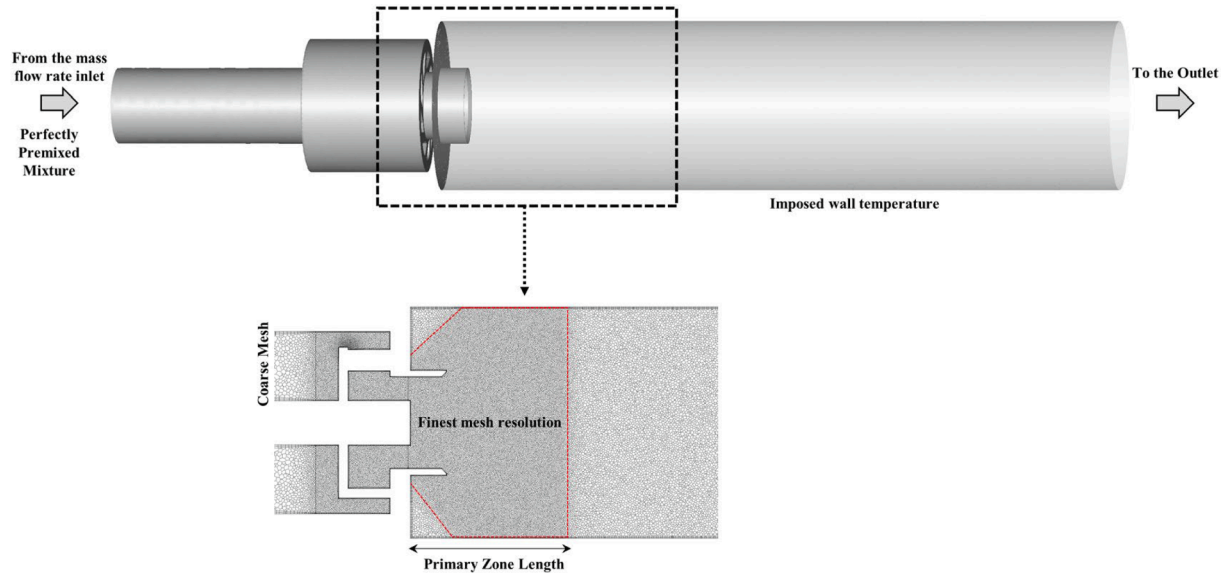

Fig. 2. Top: portion of the computational domain from the perfectly premixed inlet up to the end of the quartz tube. Bottom: detailed view of the computational grid on the primary zone. The mesh resolution at the different locations of the model is highlighted.

different sections along the flame tube to retrieve a simplified temperature profile. These experimental data are used to set the proper thermal boundary conditions at the walls of the CFD model in order to properly quantify the heat loss. At this regards, it must be specified that no secondary air is used for external cooling.

Regarding the operating conditions, Table 1 summarizes the main information of the three investigated test points, including the laminar properties like the flame speed and thickness assessed through a freely propagating flame using the same skeletal chemistry derived for this study that will be presented in a following paragraph. In addition to the fuel composition, also the temperature of the combustion air and the global equivalence ratio are kept constant during the test. Since the fuel gas has 75 % H2 vol., the equivalence ratio is in the very lean side of the mixture to contain the flame temperature, ensure the operability of the rig (i.e., avoid flashback/flame holding) and limit the NOx emission as much as possible. A modest operating pressure sweep is performed: while it doesn't affect the flame morphology significantly, the impact onto the NOx is not negligible as it will be seen in the 'Results and Discussion' section and it allows a deeper analysis on the influence of the pressure itself onto the main formation/consumption paths. Unfortunately, the covered range of pressure is not sufficient to find the value at which the NOx reaches the lowest emission for the investigated combustion system.

2. Numerical models

2.1. Combustion model and numerics

The TFM is used in the present paper as combustion model [21]. The adoption of this approach is fully justified by the perfectly premixed nature of the test rig. From a mathematical standpoint, the transport equation of the generic scalar φ (i.e., species mass fraction) can be written in this context according to Eq. (1):

$$\frac{\partial \overline{\rho}\,\widetilde{\varphi}}{\partial t}+\frac{\partial \overline{\rho}\,\widetilde{u_j}\,\widetilde{\varphi}}{\partial x_j} = \frac{\partial}{\partial x_j}\left(\overline{\rho}(EFD + (1-\Omega)D_t)\frac{\partial \widetilde{\varphi}}{\partial x_j}\right)+\frac{E}{F}\dot{\omega}(\widetilde{\varphi}) \tag{1}$$

where E, F and Ω are the efficiency function, the thickening factor and the flame sensor, respectively. The idea behind this combustion model is to artificially thicken the flame front thermal thickness by increasing the species diffusivity (multiplied by the thickening factor) in order to resolve the species profiles, including the radicals, in the actual mesh resolution. The flame sensor is defined to detect the actual flame location and apply the artificial thickening only inside the flame brush, leaving the species diffusivity unaltered elsewhere. The flame front is identified through a single reaction, involving hydrogen and radical OH, namely $H_2 + OH <=> H + H_2O$. The corresponding reaction rate is then used to calculated Ω according to Eq. (2):

$$\Omega = \tanh\left(\beta\frac{\left|\overline{\dot{\omega}_i}\right|}{\max\left(\left|\overline{\dot{\omega}_i}\right|\right)}\right) \tag{2}$$

with β a model constant equal to 10.

The chemical source term $\dot{\omega}(\widetilde{\varphi})$ is scaled by the same factor with the goal of preserving the laminar flame speed that ultimately controls the fuel consumption in a perfectly premixed flame. The maximum thickening factor (F_{max}) is calculated considering a number of points in the flame thickness (N); its value depends on the characteristic size of the mesh (Δx) and the value of the LFT (Eq. (2):

$$F_{max} = \frac{\Delta x\, N}{LFT(\Phi)} \tag{3}$$

Based on this value, the dynamic thickening factor that allows the application of the artificial thickening only where the flame front is located [22] is calculated as (Eq. (3):

$$F = \Omega(F_{max}-1)+1 \tag{4}$$

with the flame sensor Ω calculated through the reaction involving hydrogen with the radical OH, the best to detect the flame front location. The thickening of the flame front has, as direct consequence, an underestimation of the wrinkling of the flame front itself: to overcome this limitation, the efficiency function by Colin et al. [21], calculated according to Eq. (4), is employed:

$$E = \frac{1+\alpha\Gamma_0\,\frac{u'_{\Delta_e}}{s_l^0}}{1+\alpha\Gamma_1\,\frac{u'_{\Delta_e}}{s_l^0}} \tag{5}$$

with the dilatation-free velocity at the test filter u'_{Δ_e} calculated leveraging the formulation presented by Durand et al. [23], using a scale similarity assumption (Eq. (5):

$$u'_{\Delta_e} = c\Delta|\nabla\times\widetilde{\boldsymbol{u}} - \nabla\times\widehat{\widetilde{\boldsymbol{u}}}| \tag{6}$$

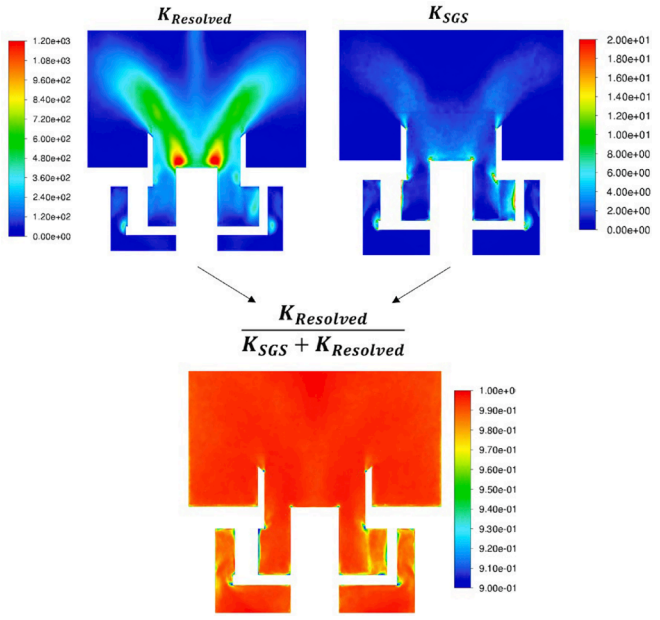

Fig. 3. Contour plot of the Pope's criterion [25] inside the swirler and the primary zone calculated as the ratio of the resolved turbulent kinetic energy over the total.

The calculation of Eq. (5) is implemented by the authors in the commercial code Ansys Fluent through a dedicated UDF. As explained above, the mesh resolution plays an essential role: it has not only to solve most of the turbulent length scales as required by the LES model, but it directly influences the flame modelling, altering the artificial thickening factor [24]. Since no automatic mesh refinement strategy is adopted in the present study, the mesh resolution is designed considering the most demanding case, i.e. TP3, that is characterized by the lowest flame front thickness being at the highest operating pressure. Fig. 2 shows a detailed view of the computational grid in the primary zone of the flame tube where the flame gets stabilized. Here and inside the radial swirler, the mesh resolution is equal to 600 μm. Considering a number of points N used to discretize the flame front equal to 9 and the values of flame front thickness reported in Table 1, according to Eq. (2), the maximum thickening factor is about 4 at the highest pressure. Such value of the thickening factor represents a typical number recommended in literature [25].

The flame tube outside the primary zone till the outlet of the computational domain (placed at the same location where the sampling probe is mounted in the rig) has a mesh size two times higher than the finest resolution while no refinement is adopted in the premixing duct. Such mesh strategy leads to a total cell count of about 13 polyhedral elements. This discretization is able to contain the CFL number below 1 adopting a time step size of $o(-5)$ and ensure that the resolved portion of the turbulent kinetic energy is well above 90 % of the total, as prescribed by the Pope's criterion [26] whose contour plot is reported in Fig. 3. The modelling of the sub-grid scales is treated according to the dynamic-Smagorinsky formulation [27].

Regarding the boundary condition set, a pressure outlet with non-reflecting boundary is adopted at the exit of the domain while a mass flow rate is imposed at the inlet specifying the mole fraction of NH_3 and H_2 inside the air. The thermal boundary condition at the quartz is defined imposing the temperature measured on the cold side, an estimated convective heat transfer coefficient and the quartz thickness. The same approach is adopted also for the dome and the burner rim. All the transport equations, including the ones related to the chemical species, are discretized at the second order as well as the implicit time-advancement.

2.2. Reduced chemistry set and its validation

TFM with detailed chemistry can be enable in a computationally affordable way only if the chemical mechanism is reduced to a skeletal size. To develop this investigation, a customized mechanism is derived from the detailed one presented by Ranzi et al. in [28], identified by the label CRECK in the following sections. The reduction is performed using a freely propagating flame as canonical case representing the most appropriate choice since the rig is perfectly premixed. Such laminar flame is calculated along a parametric study varying two main parameters, the equivalence ratio (ER equal to 0.25 and 0.5) and the operating pressure (1 and 3 bar) while maintaining the temperature of the mixture to 500 K and the fuel composition equal to the experimental one. In the validation stage also other operating conditions are evaluated with the goal to verify that the skeletal mechanism doesn't lack of generality and it can be used also outside the range investigated in this paper. Three main steps constitute the reduction algorithm. The first one is the removal of the chemistry based on the $C-$ element. The second is the application of Direct Relation Graph with Error Propagation algorithm [29,30] while the last one is the Computational Single Perturbation phase [31] for the identification of the species that are in quasi-steady state conditions that are eventually eliminated.

The laminar flame speed and the NO mass fraction are selected as targets to compare the skeletal with the complete mechanism during the reduction process. The tolerances are 5 % and 2 % for the laminar flame speed and the maximum value of NO along the flame axis, respectively. These quite tight tolerances lead to a final mechanism consisting of 27 species and 154 reactions, representing a good compromise between accuracy and computational effort reduction required by the CFD model. Once the skeletal mechanism is retrieved, the OH* chemistry is

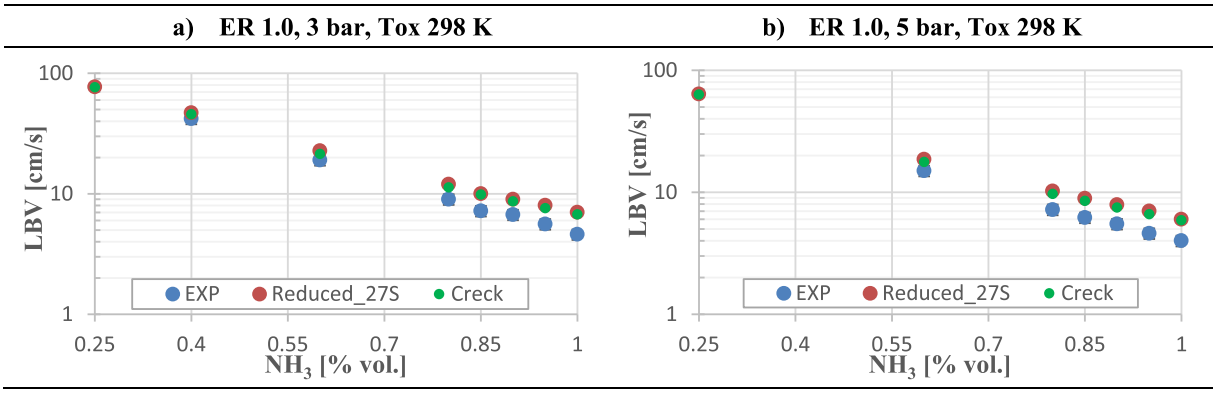

Fig. 4. Reduced mechanism validation against the CRECK and the experimental data by Ichikawa et al [33] at 3 bar (a) and 5 bar (b). Experimental data at $NH_3 = 0.25$ are missing.

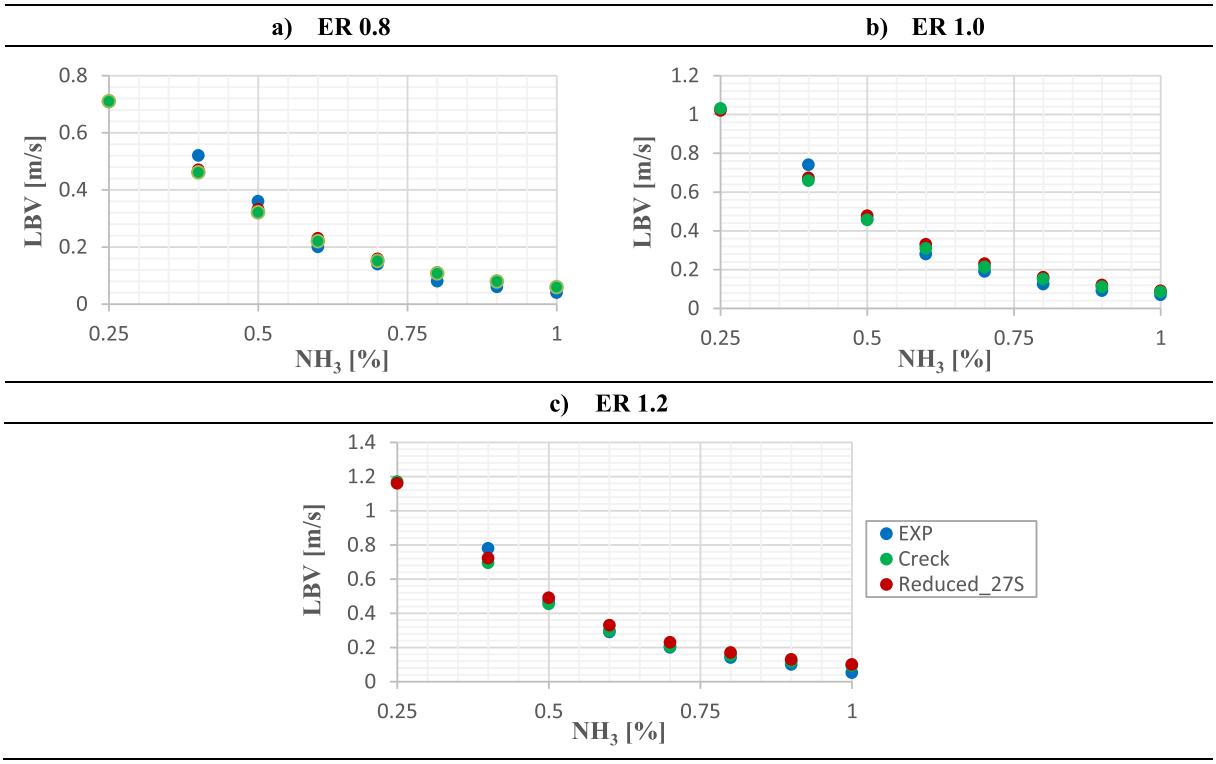

Fig. 5. Validation of the reduced chemistry against the experimetal data by Li et al. [34] and the complete mechanism at ambient conditions (298 K, p_{amb}) and equivalence ratio ranging across the stoichiometric value. Data at $NH_3 = 0.25$ are extrapolated.

added on top according to Meloni et al. [32] in order to directly compare the experimental results from the tests with the outcomes from CFD. The validation of the reduced mechanism has involved several steps along different 1D flames. Unfortunately, the lack of measurements at lean conditions or close to the experimental tests here simulated forced the validations close to stoichiometry. Fig. 4 shows the effect of both the

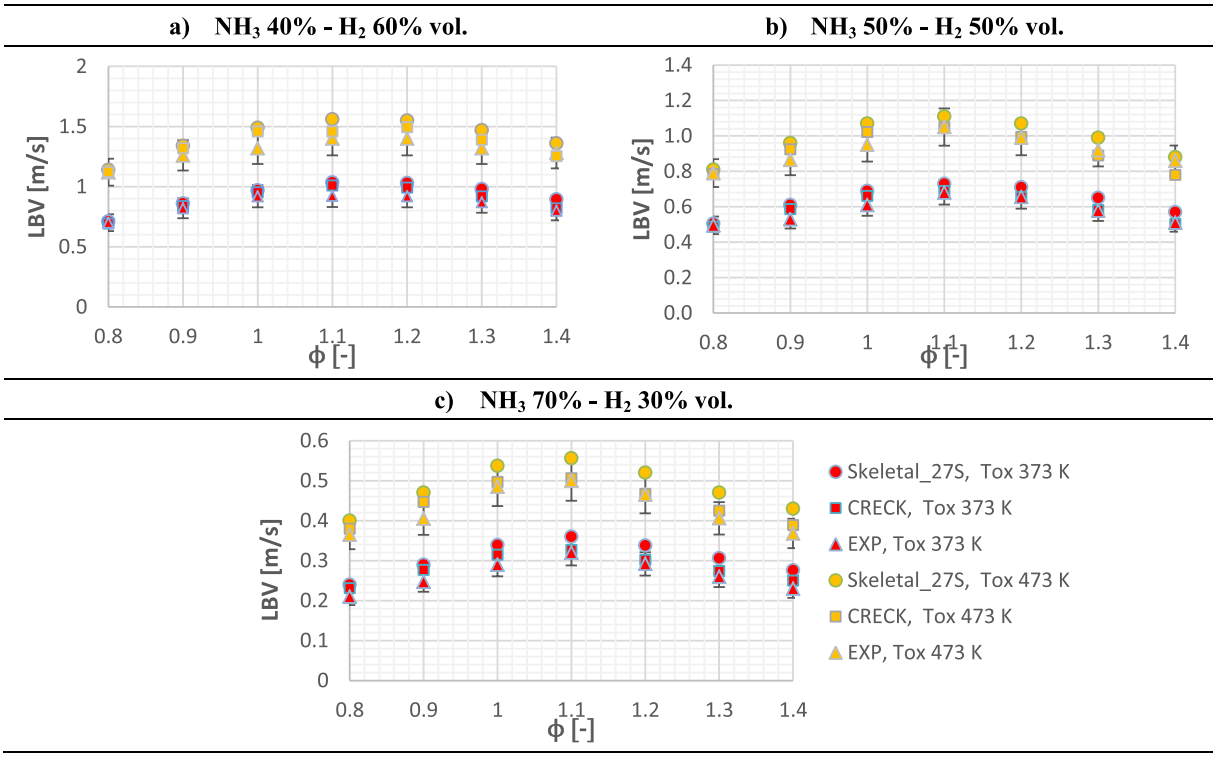

Fig. 6. LBV calculation with the skeletal and the original mechanism compared against the experimental measurements by Lhuillier et al. [35]. Data are collected at atmospheric pressure and two preheated air temperatures across the stoichiometric equivalence ratio. Three ammonia contents in the fuel are investigated: 40% (a), 50% (b) and 70% (c) by volume.

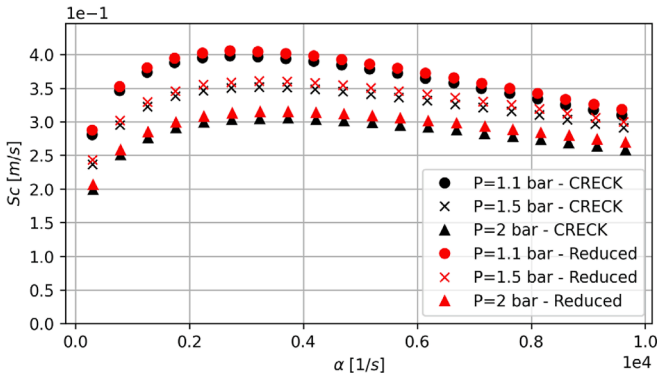

Fig. 7. Consumption speed (Sc) comparison between Reduced and detailed (CRECK) reaction mechanisms for three pressure levels (P = 1.1, 1.5, 2). The consumption speed is extracted from counterflow premixed flames in the fresh to burnt configuration increasing the strain rate level (a). The comparison refers to the operating conditions reported in Table 1.

pressure (3 bar (Fig. 4 −a) and 5 bar (Fig. 4-b)) and the NH_3 content onto the LBV predicted by the reduced mechanism, the complete mechanism and the experimental data reported by Ichikawa et al. [33]. Since the latter are limited to a NH_3 content in the fuel equal to 40 % vol., for 25 % NH_3 only the numerical results are reported. For both pressure levels the reduced chemistry is able to limit the percentage error against CRECK below 4 %, especially at lower pressure. The discrepancy decreases with the ammonia content drop, meaning that the H_2 chemistry is totally preserved: in fact, at 25 % NH_3 content the results from the two chemistry sets are practically coincident. The same trend can be observed also comparing the numerical results against the experimental data. Globally, the mean absolute difference between the data and the reduced mechanism is equal to 3 cm/s and 2.7 cm/s at 3 bar and 5 bar, respectively.

Fig. 5 reports the comparison in terms of LBV between the skeletal model, CRECK and the data from Li et al. [33] at ambient conditions varying the equivalence ratio from 0.8 to 1.2. Approximately the same level of difference between the two mechanisms and between the reduced chemistry with the data is achieved also on these cases. It can be observed that in all the three conditions the two mechanisms slightly overpredict the data until ER equal to 0.5, while under leaner conditions the numerical LBV is slower than the experiments. Overall, even considering that the reduction process is performed in lean conditions, the reduced chemistry behaves well against the selected experimental data till stoichiometric conditions.

In order to verify the reliability of the reduced mechanism in terms of laminar flame speed prediction, a last series of freely propagating flames is performed at ambient pressure and at two levels of temperature of the oxidizer (close to be relevant for GT application). Experimental data from Lhuillier et al. [35] at three levels of ammonia blended with hydrogen (40 %, 50 % and 70 % vol.) varying the equivalence ratio are leveraged for comparison (Fig. 6). While the difference among the two chemistry sets can be considered negligible, the mean absolute difference between the skeletal mechanism and the data reaches its peak of 0.1 m/s in the case with 40 % NH_3 at the highest temperature of the air. Considering that the predicted values fall for most of the equivalence ratios within the uncertainty range of the experiment, the reduced chemistry can be considered strongly reliable, at least for the simulation of perfectly premixed/partially-premixed flames. The generality of the mechanism can also be demonstrated through the response of the LBV against the strain rate.

For this reason, a premixed counterflow flamelet validation of the reduced mechanisms is performed, and the results are reported in Fig. 7. In the figure, the flame consumption speed (Sc) is reported as a function of the strain rate for different pressure levels corresponding to the conditions reported in Table 1. The prediction of the reduced

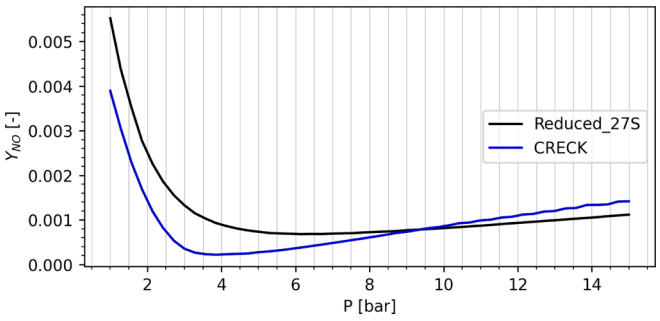

Fig. 8. NO emissions comparison between the detailed mechnaism (CRECK) and the reduced mechanism. Results extracted from a PSR + PFR reactor network reproducing the overall combustion chamber residence time. The comparison refers to the operating conditions reported in Table 1.

mechanism is perfectly in agreement with the detailed kinetics scheme all over the strain rate range investigated, demonstrating the effectiveness of the mechanism in the prediction of the change in the consumption speed induced by the stretch.

Finally, since the prediction of the NO emissions is particularly interesting with NH3, a validation of the NO emissions is reported in Fig. 8. The NO emissions have been estimated with a reactor network that includes a series of PSR (Perfectly Stirred Reactor) and a PFR (Plug Flow Reactor). The residence time in the PSR is estimated assuming the lowest residence time that allows the reaction sustainment, while the total network residence time is estimated considering a flow through time of the computational domain presented in the previous section. The comparison between the detailed and the reduced chemical mechanism reported in Fig. 8 shows an agreement that is not perfect in terms of numerical values. However, the trend for the NO emissions is perfectly captured by the reduced mechanism.

3. Results and discussion

3.1. Flame shape validation

Fig. 9 shows the comparison between the time-averaged LES (left) and the experimental Abel-deconvoluted (right) OH* map for each condition. In the figure, each contour plot is normalized against its own maximum value. In both cases, the flame length is detected by the furthest point from the burner exit belonging to the *iso*-line of the OH* mass fraction/OH* intensity having the 5 % of the peak value. The experimental OH* fields are post-processed such that the *iso*-line is retrieved only for x-coordinates higher than 20 mm to avoid the noise present close to the combustor axis created by the numerical algorithm used for the deconvolution. Experimentally, the flame elongation is subjected to a modest shortening as the pressure rises is not that huge. The numerical model is able to capture the overall flame length for the first two operating conditions while for TP3 no further flame length reduction can be observed: in fact TP3 is the only condition where the numerical flame length is even higher than the experimental one. In any case, the difference between the predicted flame length and the experimental one is of the order of few millimeters.

For what concern the flame-wall interaction, the numerical model generally under-estimates the distance of the flame front by the wall. Again, the 5 % OH* *iso*-line is leveraged to calculate this parameter, identified by the point on this curve at the minimum distance from the wall. While no discrepancy is found for TP1, TP2 is affected by about 5 mm of distance compared to the measurements. A lower discrepancy is found for TP3, with 2 mm of underprediction.

The chemiluminescence maps show that the location where the OH* reaches the peak is subjected to a small change of position while the extension of the region where the heat release rate is close to the maximum value slightly grows with the pressure rise. The latter trend

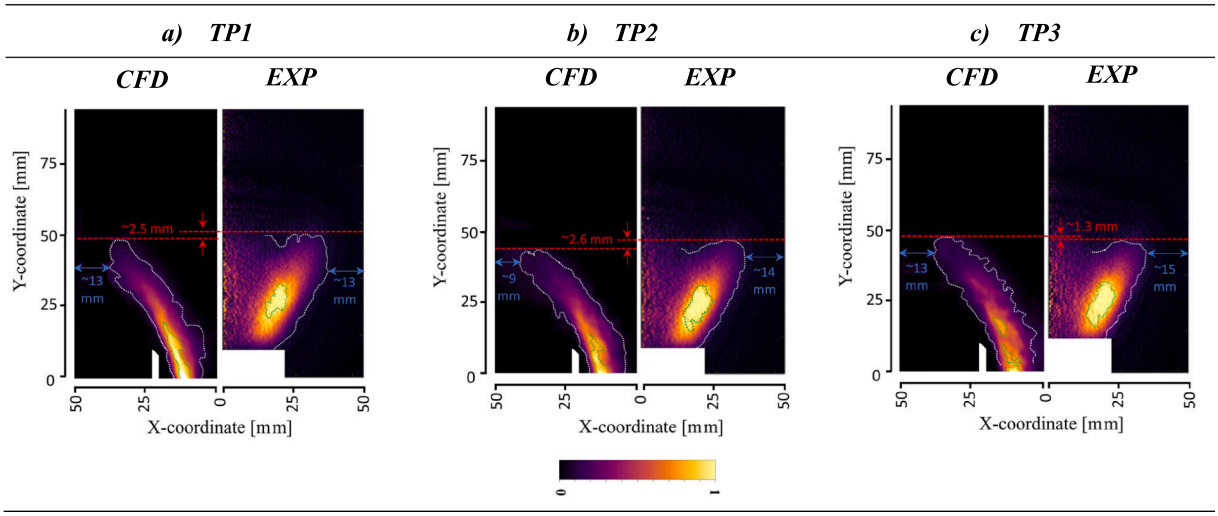

Fig. 9. OH* mass fraction from LES vs Abel-deconvoluted OH* map from the test with the pressure rising from TP1 (a) to TP3 (c). The white and the gree *iso*-line represent 5% and 90% of the maximum value, respectively.

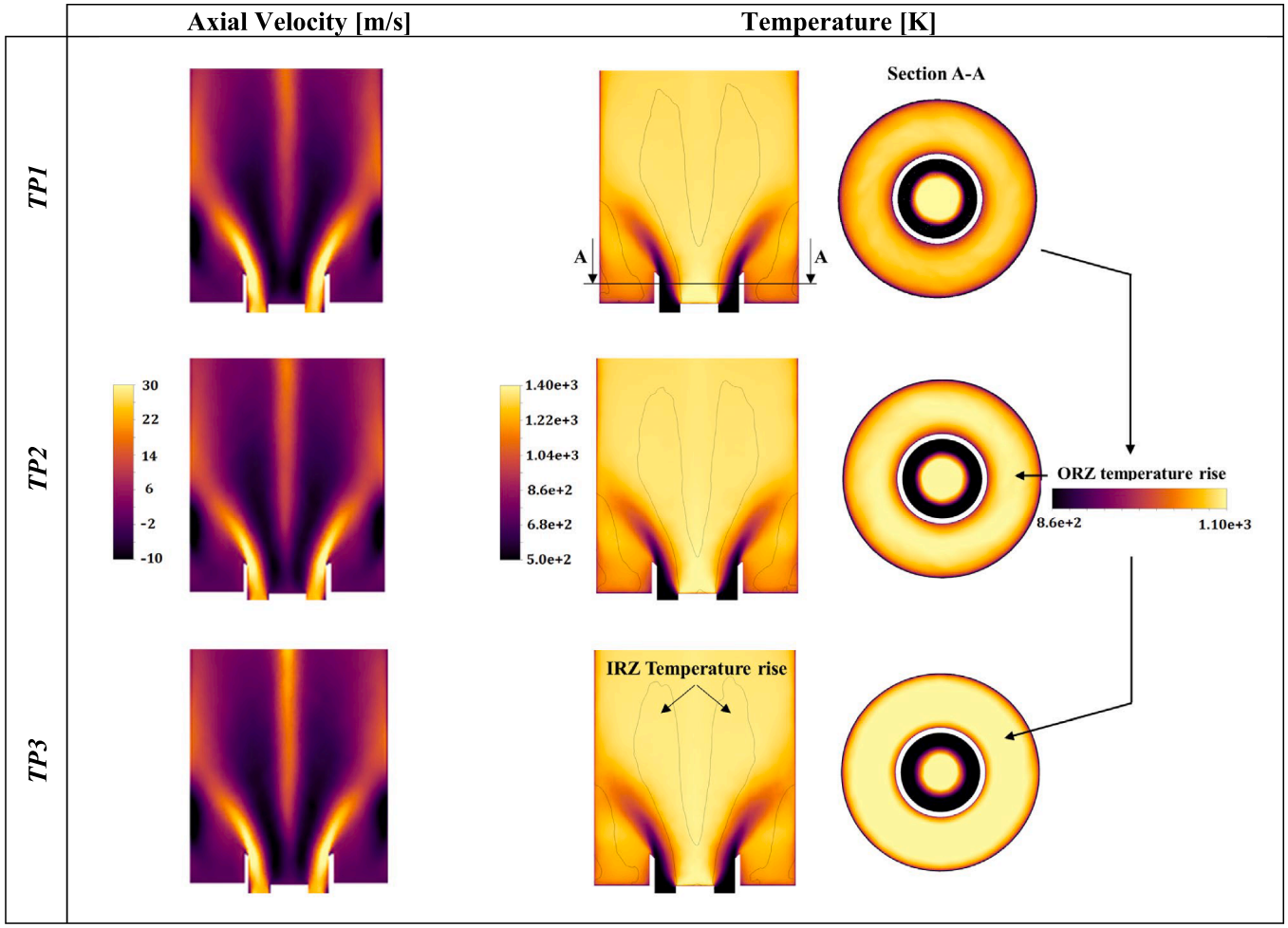

Fig. 10. Time average axial velocity (a) and temperature (b) on the mid-plane. A cross section showing the ORZ 10 mm downstream the burner exit is also reported for the temperature field. The *iso*-lines are related to the axial velocity at 0 m/s.

can be measured isolating the regions having OH* intensity higher than 90 % of the maximum value, identified by the green *iso*-lines in Fig. 9. Numerically, it is not possible to reproduce the same behavior. The overall thickness of the flame front becomes progressively higher in radial direction for TP2 and TP3 with respect to TP1 that is characterized by a quite thin region but. But, regarding the extension of the region at the highest heat release rate, the same trend observed experimentally cannot be identified. Lastly, the numerical model can reasonably reproduce the anchoring mechanism of the flame, located at the inner shear layer within the IRZ while no heat release can be detected on the ORZ side.

The shortening of the flame when increasing the operating pressure

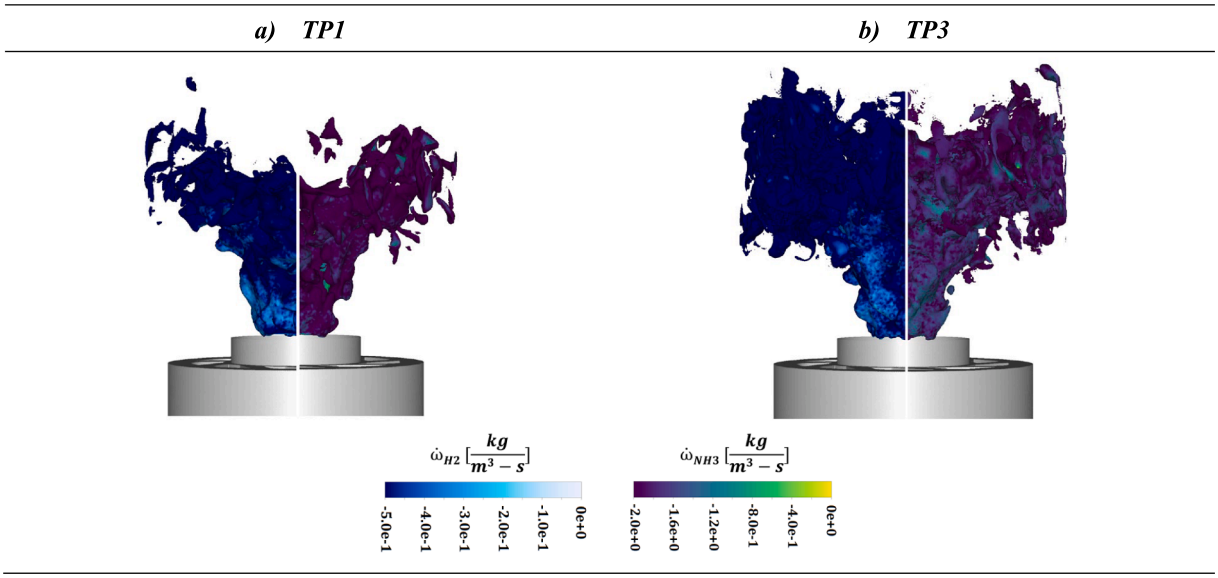

Fig. 11. Contour plot of H_2 (left) and NH_3 (rigth) consumption rate plotted on the istantaneous *iso*-surface of 10% of the maximum heat of reaction value for TP1 (a) and TP3 (b).

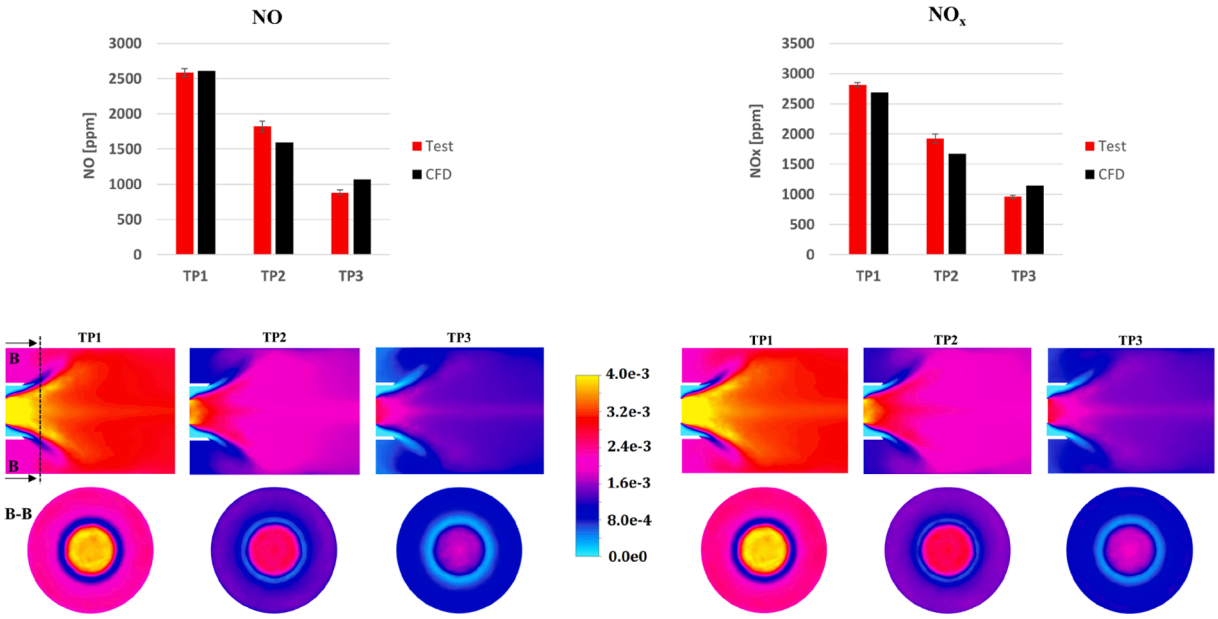

Fig. 12. NO (left) and NO_x (right) emissions: LES-TFM vs experimental data. Contour plots are extracted on the primary zone in the middle plane and in a cross section located 10 mm after the burner lip.

can be related to the higher reactivity of the mixture but also to the lower specific heat loss of the system, as investigated by Vigueras-Zuniga et al. [36] and analyzed through Fig. 10, reporting the time-averaged thermal field at different locations for all the three operating conditions as well the axial velocity field. The temperature plots on the cross section plane (A-A) show that the temperature inside the ORZ is subjected to increase: here, the heat loss has the highest impact due to the presence of both the quartz and the dome plate. Such temperature rise can be only attributed to the lower specific heat loss rising with the pressure, being all the other parameters kept constants.

Additionally, it can be seen that also the temperature within the IRZ, identified by the *iso*-line of the axial velocity at 0 m/s, increases with the pressure. As previously mentioned, such behavior is the consequence of the higher heat of reaction at higher pressure as shown in Fig. 11 where the instantaneous *iso*-surface of the 10 % of the maximum value is plotted.

In order to better highlight the differences with the pressure rise, TP2 is not reported in the figure. It is evident that TP3 is characterized by a higher extension of the *iso*-surface in the axial direction within the IRZ exactly where the higher temperature distribution can be identified. On the other side, no significant differences can be noticed in terms of maximum fuel consumption rate of the fuels.

3.2. NO_x emissions

The comparison in terms of NO_x emissions between the TFM model and the experiments is summarized in Fig. 12 where the results are split for NO and NO_x, the latter calculated as $NO + NO_2$ in agreement with the test data. The confidence interval of the measurements reported in the graphs is calculated as standard deviation from the time history of each condition. The numerical model is able to achieve a very limited discrepancy with the data for TP1 and TP2: the percentage error is of about −1% in terms of NO and −4.4 % for NO_x for the former and about −12.5 % for both NO and NO_x for the latter. The difference is larger for

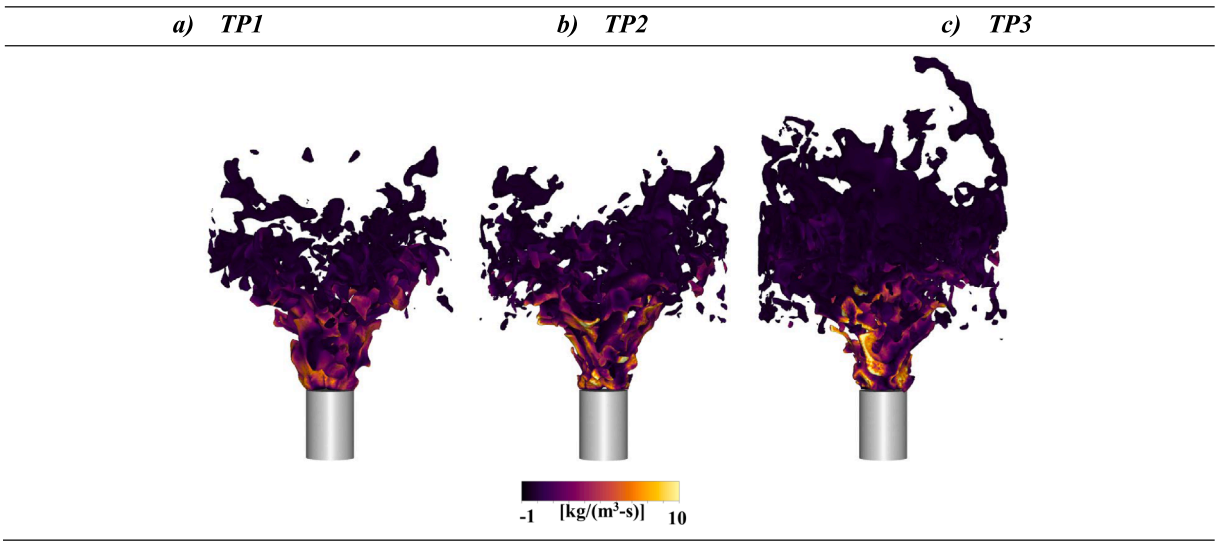

Fig. 13. Instantaneous *iso*-surface of temperature @ 1250 K colored by the NO production/consumption rate. The reburn path contributes to reduce NO emission with the pressure rise.

TP3, which is affected by an overprediction of ~ 20.5 % for both emissions. Despite this mis-prediction of the pressure rise effect onto the NO_x emission, the CFD model seems to be quite robust in reproducing the tests.

The contour plots reported in Fig. 12 are related to the primary zone of the combustor through the longitudinal middle plane and a cross section at 10 mm downstream the end of the burner lip. According to the position of the flame, the maximum emission concentration is confined by the inner shear layer right downstream the central lance where the ammonia molecule is broken. Since the combustor is operated in fully premixed mode and very low equivalence ratio, all the measured NO_x can be associated to the fuel-bound pathways.

Interestingly, rising with the pressure, the regions at the highest NO_x concentration seems to interact more with the IRZ: the contour plots of TP2 and TP3 show an enhanced transport of NO downstream the primary zone due to a stronger recirculation that can be detected through the central V-shape *iso*-line at $V_x = 0$ located in the middle of the flame tube, according to Fig. 10. Here it can be observed that the IRZ moves back toward the central lance increasing the operating pressure and, for TP2 and TP3, it is able to reach the region at the maximum NO concentration that is eventually transported far from the swirler. This explains the more intense high-NOx streak visible along the axis of the combustor for TP2 and TP3. Such finding is in agreement with previous analyses [19] where the interaction of vortical structures with high NO concentration regions within swirling flows is investigated.

Fig. 13 shows the *iso*-surface of temperature at 1250 K colored by the NO production/consumption rate for the three operating conditions. First of all, it can be seen that this surface is almost entirely confined in the region interested by the IRZ and its surface extension rises with the pressure, as previously discussed. More interestingly, it can be observed that the NO formation region gets slightly elongated with the pressure rise with higher and higher peak values from TP1 toward TP3. Conversely, the latter condition can benefit of a much more extended NO consumption zone taking place in the post flame region that globally overcomes the formation rate and leads to an emission reduction.

From a purely kinetic perspective, a freely propagating flame calculated at the same operating conditions can be used to support the investigation about what happens in the in-flame and post-flame region. According to Fig. 14, the lower NO emission at higher pressure is justified by a lower RoP along the freely propagating flame domain after that the peak is reached: TP3 is characterized by the highest reburn *RoP* approaching the chemical equilibrium (x 5.09cm along the axis of the freely propagating flame).

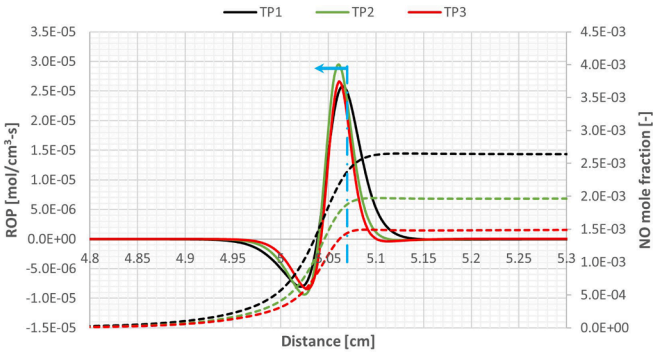

Fig. 14. X_{NO} and RoP along the freely propagating flame.

Leveraging the FPF solution, the reaction diagram showing the path from NH_3 to NO at the axial location where TP1 reaches the maximum *RoP* (blue dashed line at $x = 5.07cm$) is retrieved and presented in Fig. 15, reporting also the forward/reverse rates of the main reactions for the three simulated conditions. The most important ways NO is generated pass through a set of species (NH, NNH, NH_i, N_2, etc.) that interact with radicals (H, O and OH). The findings can be summarized as follows:

a) NO-NO2 reactions. This is the path showing the highest forward rates through radical OH: $H + NO_2 \leftrightarrow OH + NO$ and $HO_2 + NO \leftrightarrow OH + NO_2$. In particular, the role played by HO2 at the investigated conditionsis quite interesting: its formation is favored by the extra-lean conditions and favor the oxidation of NO increasing the production of radical OH and NO2. Increasing the pressure, this reaction has a forward rate that almost balances the rate of the first reaction, contributing to limit the NO formation. This does not happen at lower pressure where the rate of the first reaction is always greater than the rate of the second one.

b) *NO-N_2O reactions.* NH contributes significantly to the NO oxidation ($NO + NH \leftrightarrow H + N_2O$) and this effect increases with the operating pressure.

c) *NO-N_2 and d) NO-NNH reactions.* These paths reveal the role of NH_2 as NO oxidizer ($NH_2 + NO \leftrightarrow N_2 + H_2O$ and $NH_2 + NO \leftrightarrow OH + NNH$). The effect of the pressure rise favors the products formation: the forward rates almost double from TP1 and TP2 while a smaller increase can be observed from TP2 to TP3 for both reactions.

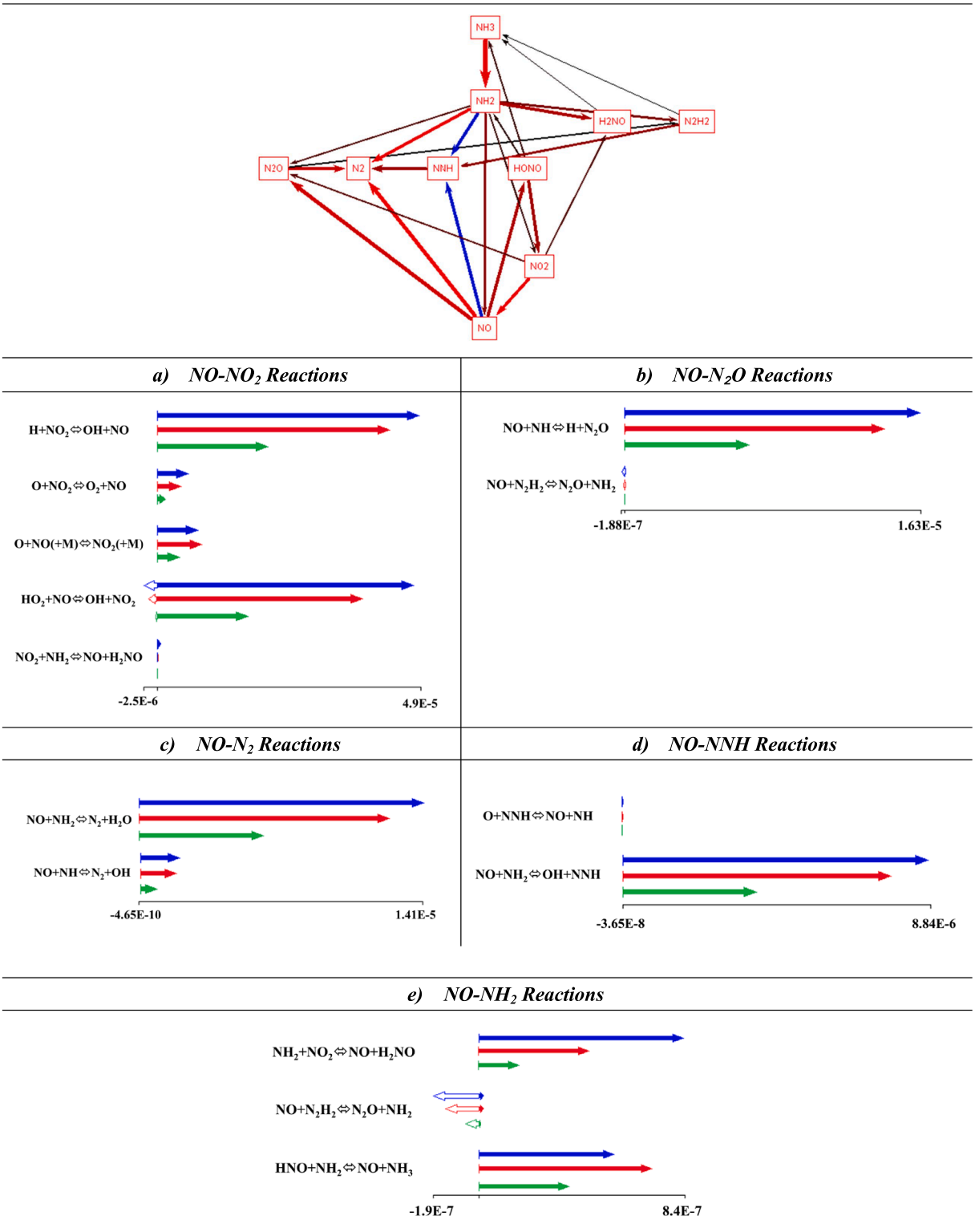

Fig. 15. Forward/Reverse reaction rates of the main paths leading to NO formation from NH_3 for the three conditions: TP1-Green, TP2-Red and TP3-Blue. (For interpretation of the references to colour in this figure legend, the reader is referred to the web version of this article.)

d) *NO-NH_2 reactions:* here NH_2 contributes to NO formation even if the production rate is much smaller compared to the above discussed paths.

As shown, radicals play a pivotal role in the identified main formation/consumption paths. The above reported *RoP* are strongly dependent by their concentrations that in turns are well-known function of the operating pressure via the third body reactions and specifically by the following reactions:

$$H + O(+M) \leftrightarrow OH(+M) \quad (7)$$

$$H + OH(+M) \leftrightarrow H_2O(+M) \quad (8)$$

with Eq. (7) having the greatest impact.

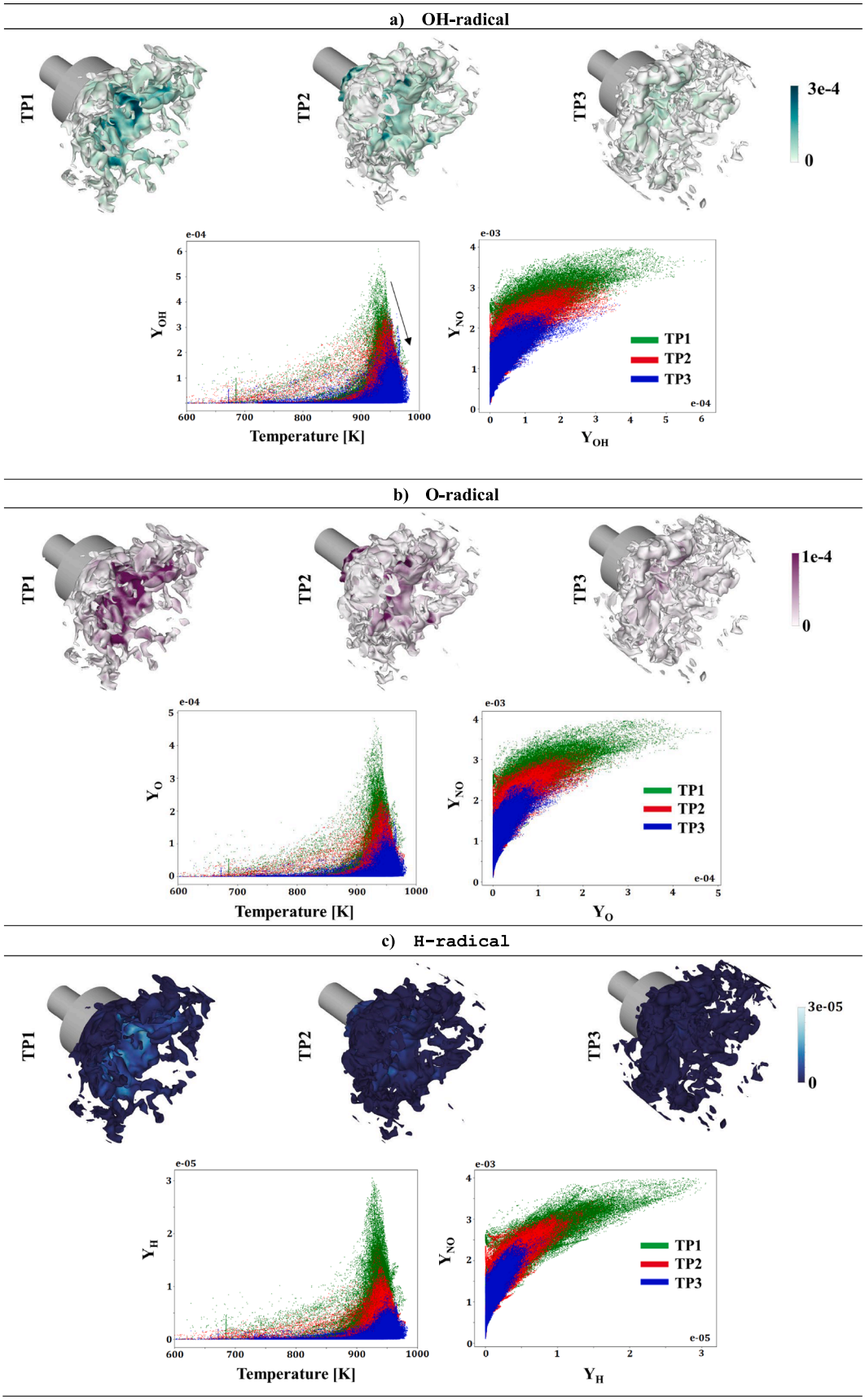

Fig. 16. Radical concentrations and scatter plots of the radicals as a function of the temperature and the NO as a function of the radicals. The data are extracted from the *iso*-surface of the progress variable at 0.8.

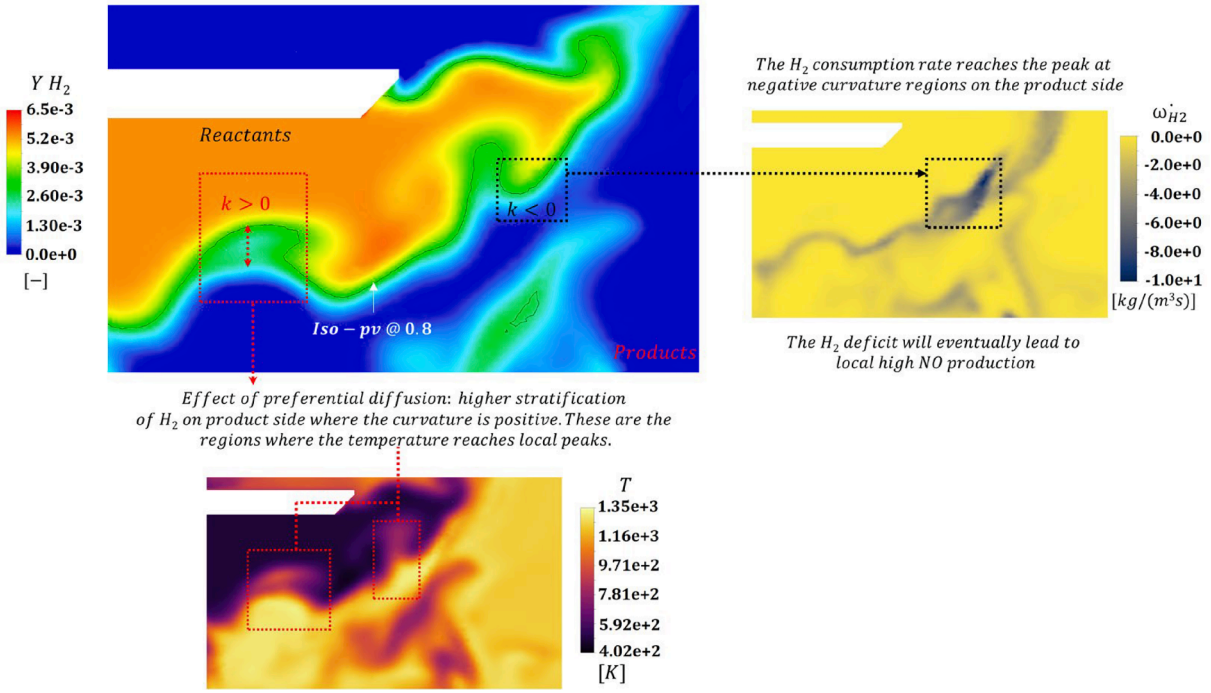

Fig. 17. Correlation between the hydrogen mass fraction and the flame front curvature impacting the hydrogen consumption rate and the temperature field as well.

With the goal to verify the role of radicals also in the CFD model, Fig. 16 shows how their concentration variation with the operating pressure. The investigation is performed on the flame front location that is here identified by the progress variable set at 0.8. The progress variable (c) is defined through the mass fraction of N_2, NO, H_2 and H_2O as follows:

$$c = Y_{N2} + Y_{NO} + Y_{H2O} - Y_{H2} \tag{9}$$

In addition to the radical concentrations, the temperature and the mass fraction of NO are also extracted from this *iso*-surface to generate the scatter plots reported in Fig. 16. Both the contour plots and the scatter plots of the radicals as a function of the temperature demonstrate how much the pressure rise leads to a significant reduction of their peak value. This behavior demonstrates that operating at higher pressure, the radicals are consumed rapidly to form H_2O, according to Eq. (7): this contributes to decrease the oxygen availability to eventually generate nitrogen oxides. As a consequence, the scatter plot of NO mass fraction as a function of free radicals results in a compact distribution placed to lower emission levels for TP3. Conversely, the cloud of points of TP1 is characterized by a higher spread over the radical concentrations coordinate. It must be also noted from both these scatter plots that most of the radicals' concentration drop happens moving from 1.1 to 1.5 bar while a more limited reduction is visible moving to 1.5 to 2 bar. As a consequence, Fig. 17 shows the same behavior in terms of NO formation/consumption rates. This means that the benefit of the operating pressure rise onto the NO reduction is probably limited only to modest

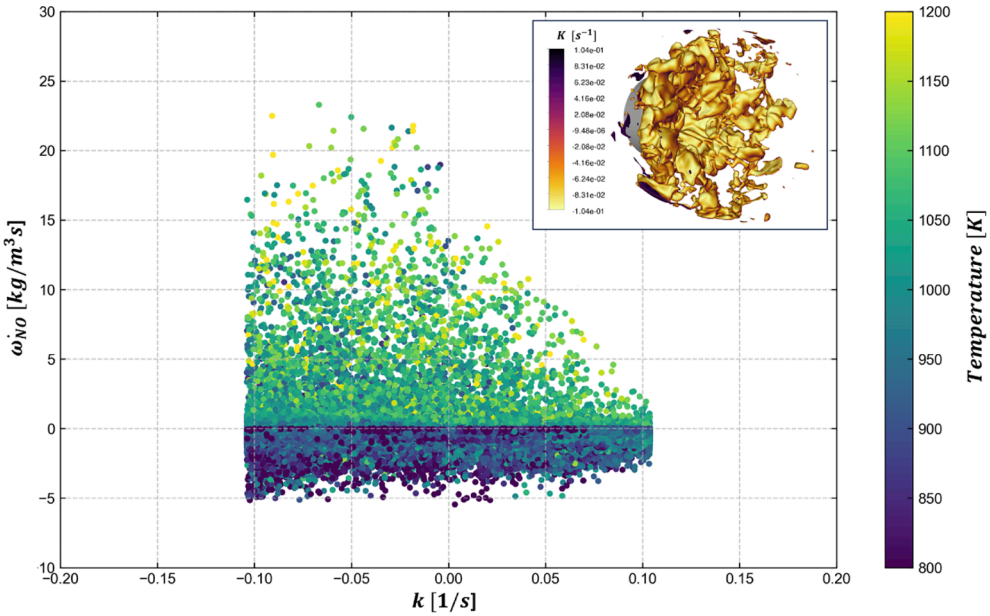

Fig. 18. NO formation rate as a function of the curvature. Data are retrieved at the *iso*-progress variable at 0.8 reported at the top-rigth parte of the image, colored by the curvature.

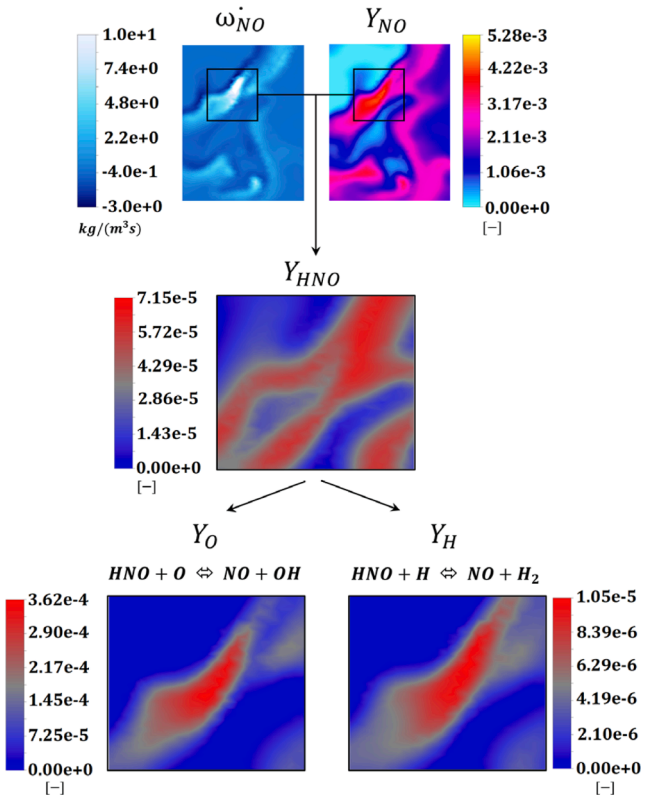

Fig. 19. Analysis of the NO formation through the HNO path in the negative curvature regions.

pressure rise and no advantage is expected at the typical values of a modern GT combustor.

3.3. Curvature *effect* on NO

According to Karimkashi et al. [37], the effects of hydrogen preferential diffusion can have an impact also on the formation of the fuel-bound NO_x. So, a more detailed post-processing will be presented in this paragraph in order to better understand this aspect. Starting from the definition of the progress variable, the curvature k is calculated as:

$$k = s_l^0 (\nabla \cdot \boldsymbol{n}) \tag{10}$$

with $n = -\frac{\nabla c}{|\nabla c|}$ being the normal vector to the flame front pointing toward the fresh reactants. Focusing the attention on TP3 (the same findings are still valid also for the other conditions), Fig. 17 reports a detailed view of the H_2 mass fraction overlapped with the progress variable *iso*-line at 0.8 in a region close to the end of the burner lip. The progress variable *iso*-line helps to visualize the regions where the flame front changes its own curvature. It can be observed that where the curvature is positive, the H_2 mass fraction becomes highly stratified since the preferential diffusion enhances the penetration in the product side. Those are the regions where temperature peaks can be detected, as reported in the corresponding contour plot. On the other hand, the regions having a negative curvature are the ones where the peak in the H_2 consumption rate is reached, as highlighted in Fig. 17.

The global relationship between the NO formation rate and the curvature is reported in Fig. 18. The scatter plot is created considering the data extracted again on the *iso*-progress variable surface at 0.8, so inside the flame front. It is found that the NO production rate increases as the curvature drops, with the highest value located at the lowest curvature. To better understand this behavior, it is useful to investigate more in detail the structure of the flame front and the role played by radicals in negative curvature regions.

At this scope, the negative curvature region highlighted in Fig. 18 is now investigated. Fig. 19, reporting both the NO formation/consumption rate and the corresponding NO mass fraction, demonstrates that the former reaches its own maximum where the H2 has the highest consumption rate, leading also to the highest NO mass fraction value on the product side. This mechanism can be explained looking at the mass fraction of HNO and the main radicals it interacts with: O and H. At this scope an even closer view is reported in Fig. 19 for such species. It is found that all the three species are at the local maxima in the region under investigation. The fast H_2 consumption in the negative curvature regions makes these radicals available for NO formation through the HNO path and, in particular, via the following reactions: $HNO + O \leftrightarrow NO + OH$ and $HNO + H \leftrightarrow NO + O + H_2$. The opposite mechanism can be identified in the positive curvature regions.

4. Conclusions

In this paper a perfectly premixed swirler fed with a blend of ammonia-hydrogen was simulated at three different levels of operating pressure leveraging the Thickened Flame Model. Firstly, a detailed chemistry set, made of 27 species and 154 reactions, has been derived and validated against experimental laminar flame speed data. Then, the performance of the CFD model has been evaluated leveraging detailed images of the flame acquired through chemiluminescence. The numerical results show a reasonable agreement with the tests in terms of flame anchoring location, flame length and distance from the walls.

More importantly, the numerical model predicts quite well the NO_x emissions, demonstrating the accuracy of the proposed approach and methodology. The post-processing was mainly focused on the sensitivity to the operating pressure of the main species involved in the NO_x formation, such as crucial radicals (OH and H), HO_2 and NH_2. In particular, it has been demonstrated how HO_2 and NH_2 have a great contribution to the NO oxidation in the ultra-lean, medium pressurized conditions here analyzed. Analogously, the impact of the third bodies in consuming the radicals and limiting the oxygen availability to form NO has been measured in the investigated flame. Lastly, the role of the preferential diffusion of H_2 in the NO formation/consumption at the flame front location has been discussed. The availability of radicals to form NO via HNO pathway is indeed influenced by the hydrogen consumption rate, that is function of the flame front curvature: the higher $\dot{\omega}_{H2}$, the higher $\dot{\omega}_{NO}$.

CRediT authorship contribution statement

R. Meloni: Writing – original draft, Validation, Supervision, Software, Methodology, Experimental camapagn. **A. Valera-Medina:** . **G. Babazzi:** Writing – original draft. **E. Pucci:** Funding acquisition. **S. Castellani:** Writing – original draft. **A. Andreini:** Supervision.

Declaration of competing interest

The authors declare the following financial interests/personal relationships which may be considered as potential competing interests: Egidio Pucci reports financial support was provided by European Union. If there are other authors, they declare that they have no known competing financial interests or personal relationships that could have appeared to influence the work reported in this paper.

Acknowledgment

This project has received funding from the European Union's Horizon 2020 research and innovation program under grant agreement No 884157.

.

Funded by the European Union

Funded by the European Union. Views and opinions expressed are however those of the author(s) only and do not necessarily reflect those of the European Union. Neither the European Union nor the granting authority can be held responsible for them.

Data availability

Data will be made available on request.

References

[1] Xiao H, Valera-Medina A, Bowen PJ. Modeling combustion of ammonia/hydrogen fuel blends under gas turbine conditions. Energy Fuels 2017;31(8):8631–42. https://doi.org/10.1021/acs.energyfuels.7b00709.

[2] Chai WS, Bao Y, Jin P, Tang G, Zhou L. A review on ammonia, ammonia-hydrogen and ammonia-methane fuels. Renew Sustain Energy Rev 2021;147. https://doi.org/10.1016/j.rser.2021.111254.

[3] Valera-Medina A, Xiao H, Owen-Jones M, David WIF, Bowen PJ. Ammonia for power. Prog Energy Combust Sci 2018;69. https://doi.org/10.1016/j.pecs.2018.07.001.

[4] Hussein NA, Valera-Medina A, Alsaegh AS. Ammonia- hydrogen combustion in a swirl burner with reduction of NOx emissions. Energy Procedia 2019;158. https://doi.org/10.1016/j.egypro.2019.01.265.

[5] Mashruk S, Kovaleva M, Chong CT, Hayakawa A, Okafor EC, Valera-Medina A. Nitrogen Oxides as a by-product of Ammonia/Hydrogen Combustion Regimes. Chem Eng Trans 2021;89:613–8. https://doi.org/10.3303/CET2189103.

[6] Valera-Medina A, Gutesa M, Xiao H, Pugh D, Giles A, Goktepe B, et al. Premixed ammonia/hydrogen swirl combustion under rich fuel conditions for gas turbines operation. Int J Hydrogen Energy 2019;44. https://doi.org/10.1016/j.ijhydene.2019.02.041.

[7] Kang L, Pan W, Zhang J, Wang W, Tang C. A review on ammonia blends combustion for industrial applications. Fuel 2023;332. https://doi.org/10.1016/j.fuel.2022.126150.

[8] Ditaranto M, Saanum I, Larfeldt J. Experimental study on high pressure combustion of decomposed ammonia: how can ammonia be best used in a gas turbine? Proc ASME Turbo Expo 2021. https://doi.org/10.1115/GT2021-60057.

[9] Ditaranto M, Saanum I, Larfeldt J. Experimental study on combustion of methane / ammonia blends for gas turbine application. Proc ASME Turbo Expo 2022. https://doi.org/10.1115/GT2022-83039.

[10] Biagioli F, Güthe F. Effect of pressure and fuel–air unmixedness on NO_x emissions from industrial gas turbine burners. Combust Flames 2007;151(1-2). https://doi.org/10.1016/j.combustflame.2007.04.007.

[11] Meloni R, Andreini A, Nassini PC. A novel Large-Eddy simulation-based process for NOx emission assessment in a premixed swirl stabilized combustion system. ASME J Eng Gas Turbines Power 2022;144(1). https://doi.org/10.1115/1.4052027.

[12] Ditaranto M, Saanum I. Experimental study on the effect of pressure on single and two stage combustion of decomposed ammonia (NH3–H2–N2) blends over a swirl stabilized burner. Combust Flame 2024;262. https://doi.org/10.1016/j.combustflame.2024.113368.

[13] Mikulčić H, Baleta J, Wang X, Wang J, Qi F, Wang F. Numerical simulation of ammonia/methane/air combustion using reduced chemical kinetics models. Int J Hydrogen Energy 2021;46(45). https://doi.org/10.1016/j.ijhydene.2021.01.109.

[14] Chaturvedi S, Santhosh R, Mashruk S, Yadav R, Valera-Medina A. Prediction of NO_x emissions and pathways in premixed ammonia-hydrogen-air combustion using CFD-CRN methodology. J Energy Inst 2023;111. https://doi.org/10.1016/j.joei.2023.101406.

[15] An Z, Zhang M, Zhang W, Mao R, Wei X, Wang J, et al. Emission prediction and analysis on CH4/NH3/air swirl flames with LES-FGM method. Fuel 2021;304. https://doi.org/10.1016/j.fuel.2021.121370.

[16] Wang C, Wang H, Luo K, Fan J. The effects of cracking ratio on ammonia/air non-premixed flames under high-pressure conditions using large Eddy simulations. Energies 2023;16:6985. https://doi.org/10.3390/en16196985.

[17] Honzawa T, Kai R, Okada A, Valera-Medina A, Bowen PJ, Kurose R. Predictions of NO and CO emissions in ammonia/methane/air combustion by LES using a non-adiabatic flamelet generated manifold. Energy 2019;186. https://doi.org/10.1016/j.energy.2019.07.101.

[18] Xiao H, Valera-Medina A, Bowen P, Dooley S. 3D Simulation of Ammonia Combustion in a Lean Premixed Swirl Burner. Energy Procedia 2017;142:1294–9. https://doi.org/10.1016/j.egypro.2017.12.504.

[19] Pugh D, Runyon J, Bowen P, Giles A, Valera-Medina A, Marsh R, et al. An investigation of ammonia primary flame combustor concepts for emissions reduction with OH*, NH2* and NH* chemiluminescence at elevated conditions. Proc Combust Inst 2021;38(4):6451–9. https://doi.org/10.1016/j.proci.2020.06.310.

[20] Valera-Medina A, Gutesa M, Xiao H, Pugh D, Giles A, Goktepe B, et al. Premixed ammonia/hydrogen swirl combustion under rich fuel conditions for gas turbines operation. Int J Hydrogen Energy 2019;44(16):8615–26. https://doi.org/10.1016/j.ijhydene.2019.02.041.

[21] Colin O, Ducros F, Veynante D, Poinsot T. A thickened flame model for large eddy simulations of turbulent premixed combustion. Phys Fluids 2000;12:1843–63. https://doi.org/10.1063/1.870436.

[22] Wang G, Boileau M, Veynante D. Implementation of a dynamic thickened flame model for large eddy simulations of turbulent premixed combustion. Combustion Flame 2011;158(11):2199–213. https://doi.org/10.1016/j.combustflame.2011.04.008.

[23] Durand L, Polifke W. Implementation of the thickened flame model for large Eddy simulation of turbulent premixed combustion in a commercial solver. Proc ASME Turbo Expo 2007;2:869–78. https://doi.org/10.1115/GT2007-28188.

[24] Rochette B, Collin-Bastiani F, Gicquel L, Vermorel O, Veynante D, Poinsot T. Influence of chemical schemes, numerical method and dynamic turbulent combustion modeling on LES of premixed turbulent flames. Combust Flame 2018;191. https://doi.org/10.1016/j.combustflame.2018.01.016.

[25] Laera D, Agostinelli PW, Selle L, Cazères Q, Oztarlik G, Schuller T, et al. Stabilization mechanisms of CH4 premixed swirled flame enriched with a non-premixed hydrogen injection. Proc Combust Inst 2021. https://doi.org/10.1016/j.proci.2020.06.378.

[26] Pope SB. Ten questions concerning the large eddy simulations of turbulent flows. New J Phys 2004;6. https://doi.org/10.1088/1367-2630/6/1/035.

[27] Lilly DK. A proposed modification of the Germano subgrid-scale closure method. Phys Fluids A 1992;4:633–5. https://doi.org/10.1063/1.858280.

[28] Ranzi E, Cavallotti C, Cuoci A, Frassoldati A, Pelucchi M, Faravelli T. New reaction classes in the kinetic modeling of low temperature oxidation of n-alkanes. Combustion Flame 2015;162(5). https://doi.org/10.1016/j.combustflame.2014.11.030.

[29] Lu Tianfeng, Law Chung K. A directed relation graph method for mechanism reduction, Proc Combustion Institute, Volume 30, Issue 1, 2005, Pages 1333-1341, ISSN 1540-7489, 10.1016/j.proci.2004.08.145.

[30] Lu Tianfeng, Law Chung K, On the applicability of directed relation graphs to the reduction of reaction mechanisms, Combust Flame, Volume 146, Issue 3, 2006, Pages 472-483, ISSN 0010-2180, 10.1016/j.combustflame.2006.04.017.

[31] Lam SH, Goussis DA. The CSP method for simplifying kinetics. Int J Chem Kinet 1994;26:461–86. https://doi.org/10.1002/kin.550260408.

[32] Meloni R, Pucci E, Mazzotta L, Borello D, Morris S, Goktepe B, et al. Large Eddy Simulations for the prediction NO_x fuel-bound NOx emissions: application to NH_3 and NH_3-CH_4 blends at different operating conditions. GT2024-123875, Proceedings of ASME Turbo Expo 2024, London UK. 2024.

[33] Ichikawa A, Hayakawa A, Kitagawa Y, Somarathne KDKA, Kudo T, Kobayashi H. Laminar burning velocity and Markstein length of ammonia/hydrogen/air premixed flames at elevated pressures. Int J Hydrogen Energy 2015;40. https://doi.org/10.1016/j.ijhydene.2015.04.024.

[34] Li J, Huang H, Kobayashi N, He Z, Nagai Y. Study on using hydrogen and ammonia as fuels: Combustion characteristics and NO_x formation. Int J Energy Res 2014;38:1214–23. https://doi.org/10.1002/er.3141.

[35] Lhuillier C, Brequigny P, Lamoureux N, Contino F, Rousselle C. Experimental investigation on laminar burning velocities of ammonia/hydrogen/air mixtures at elevated temperatures. Fuel 2020;263. https://doi.org/10.1016/j.fuel.2019.116653.

[36] Vigueras-Zuniga MO, Tejeda-del-Cueto ME, Vasquez-Santacruz JA, Herrera-May AL, Valera-Medina A. Numerical predictions of a swirl combustor using complex chemistry fueled with ammonia/hydrogen blends. Energies 2020;13:288. https://doi.org/10.3390/en13020288.

[37] Karimkashi S, Tamadonfar P, Kaario O, Vuorinen V. A numerical investigation on effects of hydrogen enrichment and turbulence on NO formation pathways in premixed ammonia/air flames. Combust Sci Technol Feb 2023. https://doi.org/10.1080/00102202.2023.2180634.